

# Dune migration and volume change from airborne LiDAR, terrestrial LiDAR and Structure from Motion–Multi View Stereo

Carlos H. Grohmann<sup>a,c,\*</sup>, Guilherme P.B. Garcia<sup>b,c</sup>, Alynne Almeida Affonso<sup>a,c</sup>, Rafael Walter de Albuquerque<sup>a,c</sup>

<sup>a</sup>*Institute of Energy and Environment, University of São Paulo (IEE-USP), São Paulo, 05508-010, Brazil*

<sup>b</sup>*Institute of Geosciences, University of São Paulo (IGc-USP), São Paulo, 05508-080, Brazil*

<sup>c</sup>*Spatial Analysis and Modelling Lab (SPAMLab, IEE-USP)*

---

## Abstract

In this work, we present an analysis of dune migration and volume change of the Garopaba dune field, southern Brazil, based on data from Airborne LiDAR (ALS - surveyed in 2010) and Structure from Motion–Multi View Stereo (SfM-MVS - surveyed in 2019). The accuracy of the SfM-MVS reconstruction was validated by a comparison between Terrestrial LiDAR (TLS) and SfM-MVS Digital Elevation Models (DEMs). Elevation differences of 2 000 random points resulted in RMSE of 0.16 m and MAE of 0.13 m, with SfM-MVS elevations slightly higher than the TLS ones. Although sand dunes are commonly regarded as a challenge to traditional photogrammetry due their homogeneous texture and spectral response, in this research image matching was successful in all areas of the survey due the presence of superficial features (footprints and sandboard tracks) and visibility of the sedimentary stratification, highlighted by heavy minerals. Displacement of dune crest lines from the ALS and SfM-MVS DEMs resulted in a migration rate of  $\approx$ 5 m/year between 2010 and 2019, in good agreement with rates derived from satellite images and historical aerial photographs of the same area. Sand volume change in the same period showed an increase of only 0.5%, which can be related to the installation of sand fences to promote dune stabilization and sand removal from the front of the dune field to keep a road open to vehicles. ALS can cover large areas in little time but its high cost still remains a barrier to wider usage, especially by researchers in developing countries. TLS has an intermediate cost but demands more fieldwork and more processing time. In our case we needed three days for the TLS survey

and around three weeks to produce a DEM of  $\approx 80\ 400\text{m}^2$ . On the other hand, we were able to cover  $\approx 740\ 900\text{m}^2$  with six flight missions in under three hours, with  $\approx 13$  hours processing time in a medium-range workstation. This makes SfM-MVS a low-cost solution with fast and reliable results for 3D modelling and continuous monitoring of coastal dunes.

*Keywords:* Aeolian Dune, DEM, SfM-MVS, UAV, ALS, TLS

---

## <sup>1</sup> 1. Introduction

<sup>2</sup> Aeolian dune fields occur in diverse depositional settings, from wet to dry (Fryberger  
<sup>3</sup> and Dean, 1979; Short, 1988; Wang et al., 2002; Livingstone et al., 2007; Martinho et al.,  
<sup>4</sup> 2010), on Earth and on other planetary bodies such as Mars, Venus, Saturn's moon Titan  
<sup>5</sup> and Pluto (Hayward et al., 2007; Radebaugh et al., 2008; Bourke et al., 2010; Kreslavsky  
<sup>6</sup> and Bondarenko, 2017; Hayes, 2018; Telfer et al., 2018).

<sup>7</sup> To better understand these dynamic environments, repeated topographic surveys of the  
<sup>8</sup> landscape are needed (Conlin et al., 2018). As the sand supply of dune fields is sensitive to  
<sup>9</sup> patterns of wind and rainfall, changes in dune field volume and morphology can be related  
<sup>10</sup> to climate change (Gaylord et al., 2001; Clemmensen et al., 2007; Sawakuchi et al., 2008;  
<sup>11</sup> Tsoar et al., 2009; Singhvi et al., 2010; Levin, 2011; Grohmann and Sawakuchi, 2013; Hoover  
<sup>12</sup> et al., 2018).

<sup>13</sup> Migration rates of aeolian dunes have been determined with aerial photographs (e.g.,  
<sup>14</sup> Finkel, 1961), orbital imagery (Shrestha et al., 2005; Potts et al., 2008; Hugenholtz and  
<sup>15</sup> Barchyn, 2010; Dong, 2015; Mendes and Giannini, 2015; Mendes et al., 2015; Bhadra et al.,  
<sup>16</sup> 2019) or Digital Elevation Models (DEMs<sup>1</sup>) (e.g., Mitasova et al., 2005b).

---

\*Corresponding author

Email addresses: guano@usp.br (Carlos H. Grohmann), guilherme.pereira.garcia@usp.br  
(Guilherme P.B. Garcia), alynne.affonso@usp.br (Alynne Almeida Affonso),  
rw.albuquerque@gmail.com (Rafael Walter de Albuquerque)

URL: <http://www.iee.usp.br>, <https://spamlab.github.io> (Carlos H. Grohmann)

<sup>1</sup>In this work we use Digital Elevation Model (DEM) in a loose sense to refer to any 3D representation of the land surface, not making a distinction between Digital Terrain Model (DTM) representing the true (bare) ground surface, or Digital Surface Model (DSM) representing a surface that does not necessarily coincide with the ground and may depict man-made structures or vegetation canopy.

17 With the growth of Geomorphometry as the practice of terrain modelling and ground-  
18 surface quantification (Pike, 1995; Pike et al., 2009; Hengl and Reuter, 2008), DEMs have  
19 became essential tools in landform analysis, as they allow speed, precision and reproducibility  
20 to calculation of geomorphometric parameters (Grohmann, 2004).

21 DEMs of aeolian dunes can be constructed by several methods such as traditional field  
22 techniques (levelling, Total Station) (Labuz, 2016), interpolation of contour lines (Judge  
23 et al., 2000; Mitasova et al., 2005b), Differential or Real-time kinematic (RTK) GPS points  
24 (Mitasova et al., 2005b; Pardo-Pascual et al., 2005), LiDAR (Light Detection and Ranging)  
25 surveys, either airborne (ALS - Airborne Laser Scanner) (Mitasova et al., 2004, 2005a,b;  
26 Baughman et al., 2018) or terrestrial (TLS - Terrestrial Laser Scanner) (Montreuil et al.,  
27 2013; Feagin et al., 2014; Fabbri et al., 2017; Bañón et al., 2019; Lee et al., 2019) and, more  
28 recently, Structure from Motion–Multi View Stereo (SfM-MVS) using images collected by  
29 handheld cameras, mounted on poles, kites or Unmanned Aerial Vehicles (UAVs) (Mancini  
30 et al., 2013; Gonçalves and Henriques, 2015; Conlin et al., 2018; Duffy et al., 2018; Seymour  
31 et al., 2018; Solazzo et al., 2018; Guisado-Pintado et al., 2019; Laporte-Fauret et al., 2019;  
32 Lee et al., 2019; O’Dea et al., 2019; Pagán et al., 2019; Taddia et al., 2019).

33 In this work, we present an analysis of dune migration and volume change of the  
34 Garopaba dune field, southern Brazil, based on DEMs from ALS (surveyed in 2010) and  
35 SfM-MVS (surveyed in 2019). Altimetric accuracy of the SfM-MVS DEM was validated  
36 by comparison with TLS data collected during the same fieldwork campaign of the UAV  
37 flights. The results show almost no change in volume and a migration rate of  $\approx$ 5 m/year,  
38 compatible with those derived from aerial and orbital imagery. The use of SfM-MVS for  
39 aeolian dunes modelling is recommended and the factors that contributed to a successful 3D  
40 reconstruction are discussed.

#### 41 1.1. Study area

42 The study area, located in Santa Catarina State, southern Brazil (Fig. 1A-B), comprises  
43 barrier-lagoon depositional systems with associated dune fields (Giannini et al., 2007) which  
44 evolved since the Middle Holocene during a phase of low-rate decreasing relative sea level

45 after a highstand of around 2.5 m above the present sea level (Angulo et al., 2006).

46 The Garopaba (or Siriú) dune field is composed of unvegetated and vegetated aeolian  
47 dunes. The unvegetated dunes are represented by mostly barchanoid chains, while the  
48 vegetated ones include parabolic dunes, blowouts and foredunes (Martinho et al., 2006;  
49 Giannini et al., 2007; Hesp et al., 2007, 2009). These dune fields are a result of wind  
50 strength intensification and sand supply increase in southern Brazilian coast during the  
51 Late Holocene (Mendes and Giannini, 2015; Mendes et al., 2015).

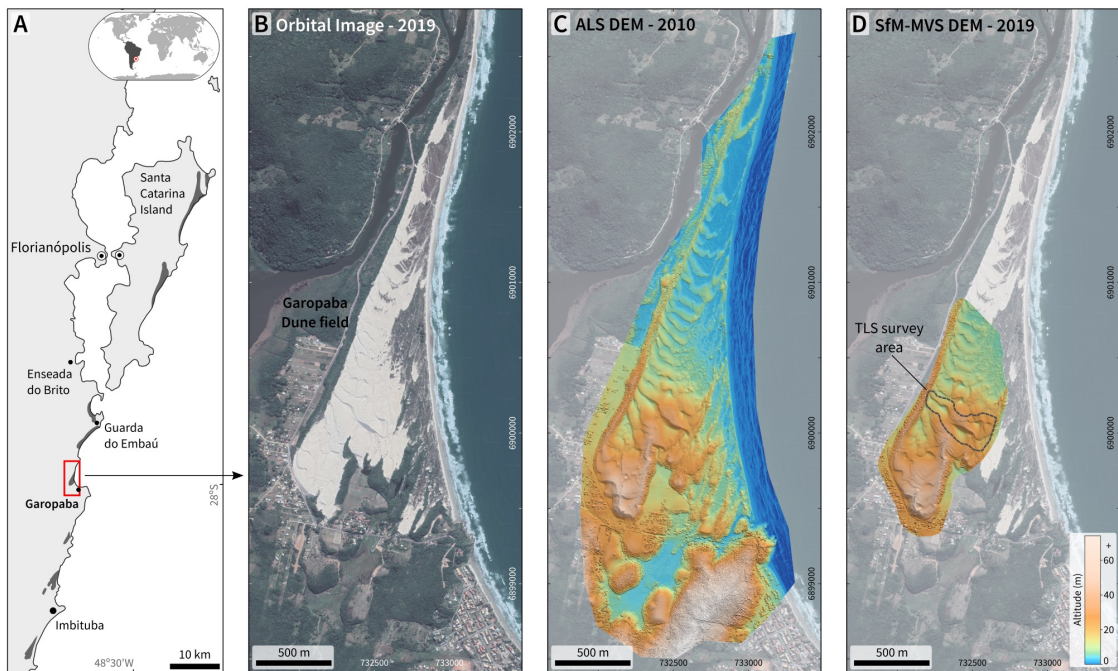


Figure 1: A) Location of study area in southern Brazil; B) Satellite image of the Garopaba dune field (image date: 07-30-2017); C) Digital Surface Model produced by Airborne LiDAR (2010); D) Digital Surface Model produced by Structure from Motion–Multi View Stereo (2019), with TLS survey area shown. Elevation colorscale is the same for C and D. Shaded relief illumination: N25°, 30° above horizon. Dune field satellite imagery ©2019 Maxar Technologies, powered by Google. Coordinate system for B/C/D and following figures: UTM zone 22 southern hemisphere, WGS84 datum.

## 52 2. Methods

53 This section presents the datasets, methods and tools used in this study. A flowchart  
54 of the analysis steps is in the Supplemental Material. Table 1 shows, for each kind of data

55 used in this paper (ALS, SfM-MVS, TLS), area of the interpolated DEM, number of points  
56 and density of points within that area.

Table 1: Overview of datasets used in this study. See text for details and Supplemental Material for maps of point density.

Data	DEM Area (m <sup>2</sup> )	# points	points/m <sup>2</sup>
ALS (full)	4 434 722	11 574 555	2.6
ALS (SfM area)	740 922	2 380 005	3.2
SfM-MVS (full)	740 922	344 595 132	465.1
SfM-MVS (thin 125 <sup>th</sup> pt)	740 922	2 376 632	3.2
SfM-MVS (TLS area)	80 413	28 158 102	350.1
SfM-MVS (10 cm grid)	80 413	8 039 750	99.9
TLS (full)	80 413	1 187 708 492	14 770.1
TLS (2 cm filter)	80 413	170 141 709	2 115.8
TLS (10 cm grid)	80 413	7 028 118	87.4

57 *2.1. Airborne LiDAR*

58 Airborne LiDAR (ALS) data were collected on October 2010 by Geoid Laser Mapping  
59 Co. using an Optech ALTM 3100 sensor with a saw-tooth scanning pattern, density of about  
60 one point per 0.5 m<sup>2</sup>, measured from an altitude of  $\approx$ 1 200 m ( $\approx$ 4 000 ft). Raw LiDAR data  
61 (with up to four laser pulses) were processed by Geoid and delivered with vertical accuracy  
62 of 0.15 m ( $1\sigma$ ) and horizontal accuracy of 0.5 m ( $1\sigma$ ).

63 ALS data (LiDAR first returns) were imported into GRASS-GIS (Neteler et al., 2012)  
64 as vector points and a DEM with 0.5 m spatial resolution was created by interpolation of  
65 the vector points with bilinear splines (Brovelli and Cannata, 2004; Brovelli et al., 2004)  
66 (Fig. 1C).

67 *2.2. Fieldwork and Ground Control Points*

68 Fieldwork for TLS and SfM-MVS surveys was conducted on February 2019. Six targets  
69 were deployed within the dune field area (Fig. 2B) and their coordinates were determined by

70 Differential Global Positioning System (DGPS), to serve as Ground Control Points (GCPs)  
71 for georeferencing the SfM-MVS outputs and the TLS point cloud.

72 Each target measured  $\approx$ 80x60 cm in a black and white checkered pattern and was clearly  
73 visible in the photos (Fig. 2C). A Spectra Precision SP60 DGPS was used in a base-rover  
74 static configuration and raw data was post-processed in Survey Office<sup>1</sup> 4.10 software, using  
75 the Imbituba Station of the Brazilian GPS Network as reference. The processing reports  
76 are available in the Supplemental Material.

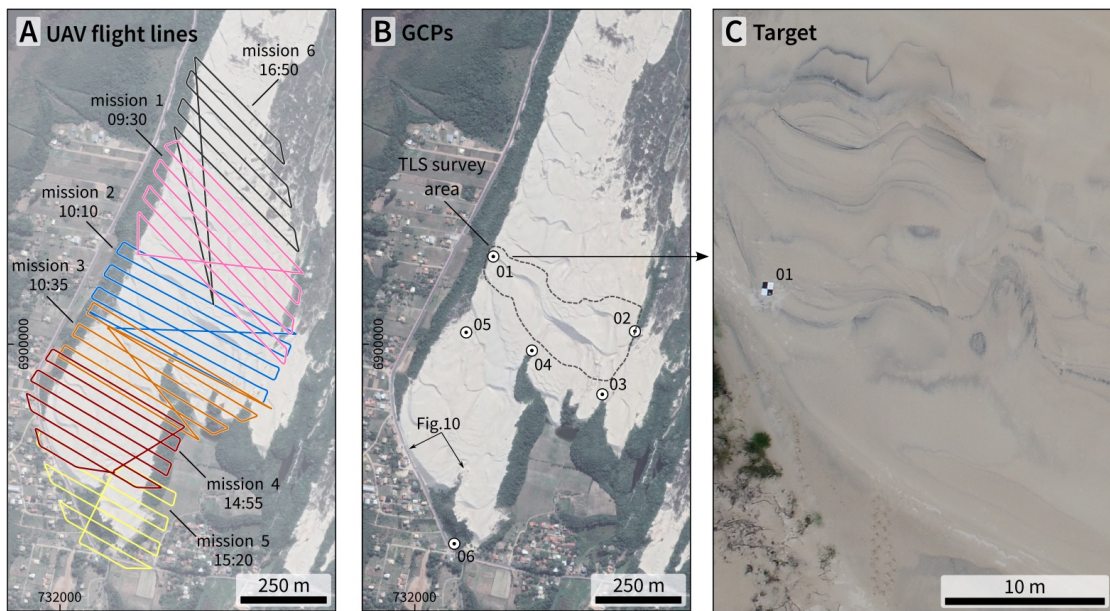


Figure 2: A) Flight missions executed over the dune field; B) Ground Control Points used to georeference the SfM-MVS outputs and TLS data; C) Target (GCP 01), sedimentary structures and superficial features seen in the UAV photo.

77 *2.3. Terrestrial LiDAR*

78 Terrestrial LiDAR (TLS) data were collected with a FARO<sup>TM</sup> Laser Scanner Focus<sup>3D</sup>  
79 S120, a geodetic laser scanner with distance measurement based on phase shift of infrared  
80 light (905 nm), maximum range of 120 m, and ranging error of  $\pm 2$  mm at 10 m distance at  
81 90% reflectivity (FARO Technologies Inc., 2013). The scanner was set at resolution of “1/5”  
82 and quality of “3x”, resulting in a point spacing of 7.67 mm at a distance of 10 m, scan time

83 of two minutes and 28.4 million points per scan (this model does not acquire images). Five  
84 spherical targets provided with the equipment were arranged on the ground at  $\approx$ 10 m from  
85 the TLS and re-positioned in a ‘leapfrog’ scheme during the survey, so that each consecutive  
86 scan was able to capture at least two spheres from the previous one. In three days of field  
87 work, 110 scans were collected, covering an area of  $\approx$ 80 400 m<sup>2</sup> (Fig. 1D).

88 TLS data were processed in FARO Scene 7.1<sup>2</sup>. Each scan was registered to its adjacent  
89 ones manually using the spherical targets as references. Since this TLS model does not  
90 carry an integrated GPS, georeferencing of the point cloud was based on two DGPS points  
91 located at the extremities of the surveyed area (Fig. 2B).

92 To overcome the heterogeneous distribution of data common to terrestrial LiDAR, with  
93 a very high density of points near the scanner, the full point cloud was subsampled in FARO  
94 Scene with a minimum distance filter of 2 cm between points. To eliminate duplicate points  
95 and compensate for small differences in the alignment of individual scans, the thinned and  
96 georeferenced point cloud was gridded to a raster in GRASS-GIS using the mean elevation  
97 value of LiDAR points within 10 cm cells (`r.in.xyz` module). To fill empty (null) cells,  
98 the raster was converted to vector and a DEM with 10 cm spatial resolution was created by  
99 interpolation with bilinear splines (Fig. 4A).

#### 100 2.4. SfM-MVS

101 Images for the SfM-MVS reconstruction were acquired by a DJI Phantom 4 Pro UAV.  
102 The aircraft digital camera has an 1” CMOS 20MP sensor, global shutter, 84° FOV and  
103 8.8 mm focal distance (24 mm at 35 mm equivalent). Images can be saved as JPEG or  
104 RAW, 5 472×3 648 px (3:2 ratio). Flight missions were planned and executed using the  
105 MapPilot app<sup>3</sup> with height above takeoff point of 100 m (image footprint 150×100 m, pixel  
106 size  $\approx$ 2.7 cm) and 75% overlap along and across-track.

107 Six missions were flown, covering an area of  $\approx$ 869 000 m<sup>2</sup> with 810 images. Figure 2A  
108 shows flight paths and starting time for each mission (UTC-3). Weather conditions during  
109 fieldwork were of dark skies with light rains scattered throughout the day.

110 The SfM-MVS workflow (e.g., [Westoby et al., 2012](#); [Viana et al., 2018](#); [James et al.,](#)

111 2019) was processed in Agisoft Metashape Pro version 1.5.1<sup>4</sup>. In the SfM step, images  
112 were aligned with ‘High’ accuracy; the MVS reconstruction was set to ‘High’ quality and  
113 ‘aggressive’ depth filtering. The processing report is available in the Supplemental Material.

114 The full SfM-MVS point cloud was subsampled (thinned) with LAStools (Isenburg, 2019)  
115 by extracting every 125<sup>th</sup> point, imported into GRASS-GIS as vector points and interpolated  
116 with bilinear splines to a DEM with 0.5 m resolution (Fig. 1D). The thinning value was  
117 determined after experimentation, and the goal was to obtain a similar number of points,  
118 within the interpolation area, for the ALS and SfM point clouds (Table 1).

#### 119 2.4.1. Accuracy of SfM-MVS DEM

120 The vertical accuracy of a DEM can be computed from the differences between the  
121 dataset being analysed and co-located values from an independent source of higher accuracy  
122 (Willmott and Matsuura, 2005; Wechsler, 2007; Hebeler and Purves, 2009; Reuter et al.,  
123 2009; Baade and Schmullius, 2016). To evaluate the accuracy of the SfM-MVS reconstruc-  
124 tion, the TLS DEM was considered as the reference.

125 The full SfM-MVS point cloud was imported into GRASS-GIS in the same manner of the  
126 TLS data: gridded by the mean elevation in 10 cm cells, converted to vector and interpolated  
127 with bilinear splines to a DEM with 10 cm resolution (Fig. 4B).

128 Mean Absolute Error (MAE) and Root Mean Square Error (RMSE) are metrics that been  
129 widely used in the Geosciences to measure the accuracy of DEMs (e.g., Nikolakopoulos et al.,  
130 2006; Willmott and Matsuura, 2006; Smith and Vericat, 2015; Gesch et al., 2016; Satge et al.,  
131 2016; Grohmann and Sawakuchi, 2013; Grohmann, 2018). MAE (Eq. 1) and RMSE (Eq. 2)  
132 were calculated from a set of 2 000 random points constrained to a mask to avoid sampling  
133 areas with vegetation or without TLS data. The number of points was determined using a  
134 Monte Carlo approach to evaluate the correlation between sets of random points extracted  
135 from the TLS DEM (see Supplemental Material).

$$MAE = \frac{1}{n} \sum_{i=1}^{i=n} (|z_{TLS} - z_{SfM}|) \quad (1)$$

$$RMSE = \sqrt{\frac{1}{n} \sum_{i=1}^{i=n} [(z_{TLS} - z_{SfM})^2]} \quad (2)$$

136 *2.5. Dune Migration and Sand volume*

137 Dune migration can be evaluated from multi-temporal data such as aerial photographs  
 138 (Finkel, 1961; Stafford and Langfelder, 1971; Mendes and Giannini, 2015; Baughman et al.,  
 139 2018), satellite images (Hoover et al., 2018; Dong, 2015; Yang et al., 2019) or LiDAR DEMs  
 140 (Mitasova et al., 2004, 2005a,b; Baughman et al., 2018). Dune migration between the 2010  
 141 (ALS) and 2019 (SfM-MVS) surveys was determined as the displacement of dune crest lines.

142 For each survey, crest lines were drawn in QGIS version 3.8 (QGIS Development Team,  
 143 2019); lines connecting the crests were draw approximately parallel to the S-SW migration  
 144 direction (Hesp et al., 2007; Mendes and Giannini, 2015) (Fig. 3) and saved in shapefile for-  
 145 mat. Azimuth and length of each displacement line were calculated with Python version 2.7  
 146 (Python Software Foundation, 2019) using the `ogr` module of the GDAL library (GDAL De-  
 147 velopment Team, 2019) to access vector geometries. Mean azimuth was calculated according  
 148 to Fisher (1993).

149 Sand volume was calculated with the GRASS-GIS `r.volume` module (Hincknorne, 1988).  
 150 This module calculates volume by summing cell values within a given area and then multi-  
 151 pling by the area occupied by those cells. An elevation of 0 m (zero) was used as a reference  
 152 base level.

153 *2.6. Data Analysis and Availability*

154 In order to streamline the process and ensure reproducibility (Barnes, 2010), data analysis  
 155 was performed in GRASS-GIS version 7.6 (Neteler et al., 2012; GRASS Development Team,  
 156 2019) through Jupyter notebooks (Kluyver et al., 2016; Rule et al., 2018) using the Pygrass  
 157 library (Zambelli et al., 2013) to access GRASS' datasets. The notebooks and associated  
 158 data files are available on GitHub<sup>5</sup> and Zenodo<sup>6</sup>. Statistical analyses were performed with the  
 159 Python libraries Scipy, Numpy, Pandas, Seaborn and Matplotlib (Oliphant, 2006; Hunter,  
 160 2007; McKinney, 2011; The SciPy community, 2013; Waskom et al., 2016).

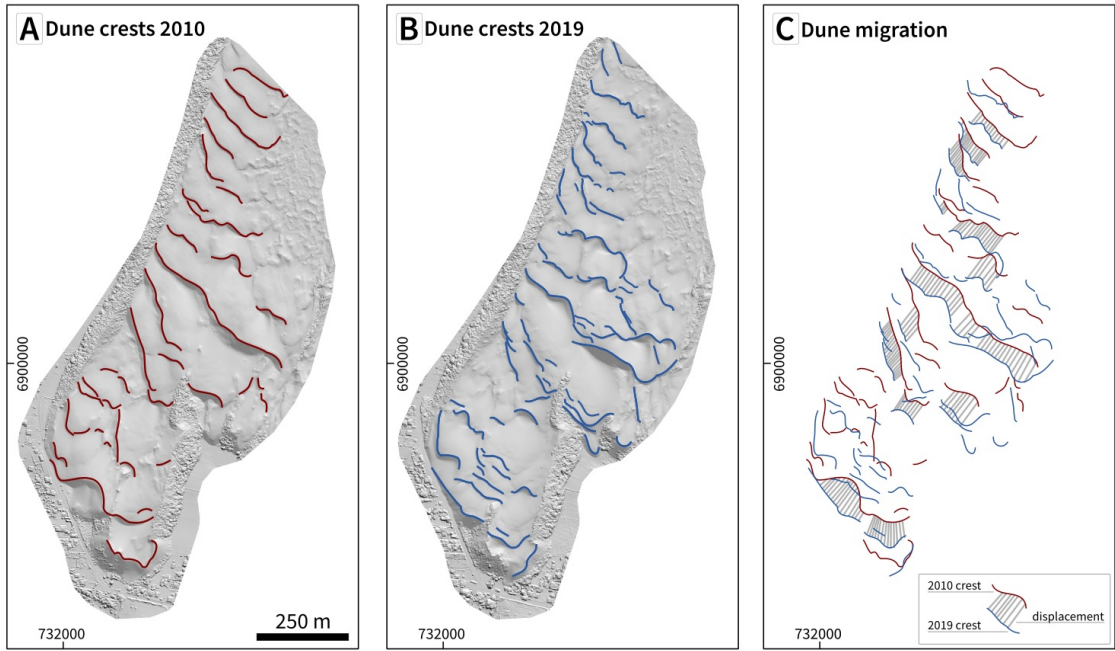


Figure 3: Determination of dune migration between 2010 and 2019 surveys. A) dune crests of 2010, over shaded relief image of ALS DEM; B) dune crests of 2019, over shaded relief image of SfM-MVS DEM; C) displacement lines (grey) connecting crest lines.

The point cloud datasets are available via the OpenTopography Facility<sup>7</sup> (Crosby et al., 2011; Krishnan et al., 2011). The following datasets were used in this study: OpenTopography ID OT.032013.32722.1 (ALS – Grohmann, 2010; Grohmann and Sawakuchi, 2013), OTDS.072019.32722.1 (SfM – Grohmann, 2019), OTDS.102019.32722.1 (TLS – Grohmann et al., 2019).

### 3. Results

#### 3.1. TLS and SfM-MVS

The DEMs produced from the TLS and SfM-MVS data are presented in Fig. 4. The surfaces are very similar, without any major difference in elevation or in the reconstruction of topographic features. Upon a closer inspection, the SfM-MVS DEM presents a small scale surface roughness not visible in the TLS DEM. To visually evaluate this difference, surface roughness of the DEMs was calculated as the standard deviation of slope (Grohmann et al.,

173 2010) in a 5x5 pixels neighbourhood ( $0.5 \times 0.5$  m).

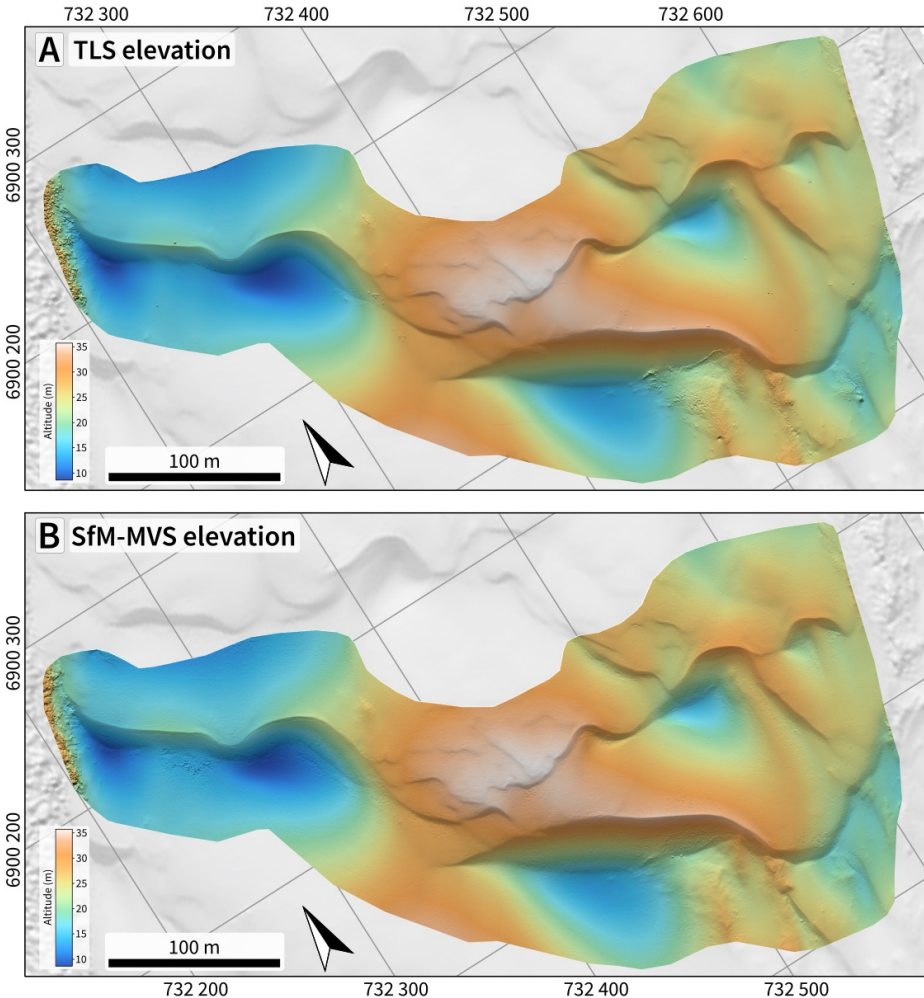


Figure 4: A) TLS DEM; B) SfM-MVS DEM. Elevation colour scale is the same for A and B. Shaded relief illumination: N $25^\circ$ , 30° above horizon.

174 The TLS DEM has a smooth surface, with higher roughness values on vegetated areas  
175 and over some of the places where the TLS equipment was positioned (Fig. 5A). These spots  
176 can be related to a small mismatch between adjacent scans, where in one there is no data  
177 (under the scanner), so the gridding procedure cannot compensate the difference and the  
178 result is a small circular patch of the terrain slightly above or below its surroundings. Dune  
179 crests are well marked by above-average roughness. Footprints and track marks are also  
180 visible, with lower roughness values.

181        The SfM-MVS DEM shows a widespread distribution of low and average roughness values  
 182        (Fig. 5B). While the dune crests can be identified, track marks are no longer visible and  
 183        the patch of vegetation near the sandboard tracks cannot be discriminated based on its  
 184        roughness. A set of footprints seen in the central-eastern portion of the TLS roughness  
 185        map is not visible in the SfM-MVS roughness because the SfM-MVS survey was carried out  
 186        before the TLS survey could cover that area.

187        Considering the scale of the dunes, the differences in roughness between the DEMs are  
 188        seen as a micro-scale feature, not affecting the goals of this research. If there is need for the  
 189        SfM-MVS surface to be smoother, a moving-window filter might be used, but sharp edges  
 190        such as dune crests will be modified as well (Grohmann and Riccomini, 2009). If the sharp  
 191        edges must be preserved, despeckling procedures (e.g., Sun et al., 2007; Stevenson et al.,  
 192        2010) should be employed.

193        The vertical accuracy of the SfM-MVS DEM was calculated from a set of 2 000 random  
 194        points (Fig. 6A), resulting in RMSE of 0.16 m and MAE of 0.13 m. Descriptive statistics  
 195        of the TLS and SfM-MVS DEMs are very similar (Table 2), with slightly higher values of  
 196        minimum, mean and median for the SfM-MVS DEM.

197        Elevation differences between the DEMs range from -0.62 m to +0.23 m, with mean  
 198        of -0.10 m and standard deviation of 0.13 m. A scatterplot of elevations (TLS × SfM-  
 199        MVS, Fig. 6B) shows minimal dispersion of points, with an  $R^2$  of 0.999 (see Supplemental  
 200        Material). The histogram of differences (Fig. 6C) has a bimodal distribution, with  $\approx 73\%$  of  
 201        the values below zero, indicating that, in general, the SfM-MVS DEM has higher elevations  
 202        than the TLS DEM, and the boxplot of differences (Fig. 6D) shows that only 11 points are  
 203        classified as outliers, with values below -0.5 m.

Table 2: Descriptive statistics of the TLS, SfM-MVS DEMs and of differences.

	min	max	mean	median	std.dev.	skewness	kurtosis	25%quant.	75%quant.
TLS	8.518	36.128	23.749	24.641	6.436	-0.217	-0.749	18.238	28.247
SfM-MVS	8.684	36.104	23.849	24.796	6.410	-0.231	-0.755	18.393	28.327
Diff.	-0.623	0.226	-0.100	-0.103	0.129	-0.259	0.119	-0.196	0.007

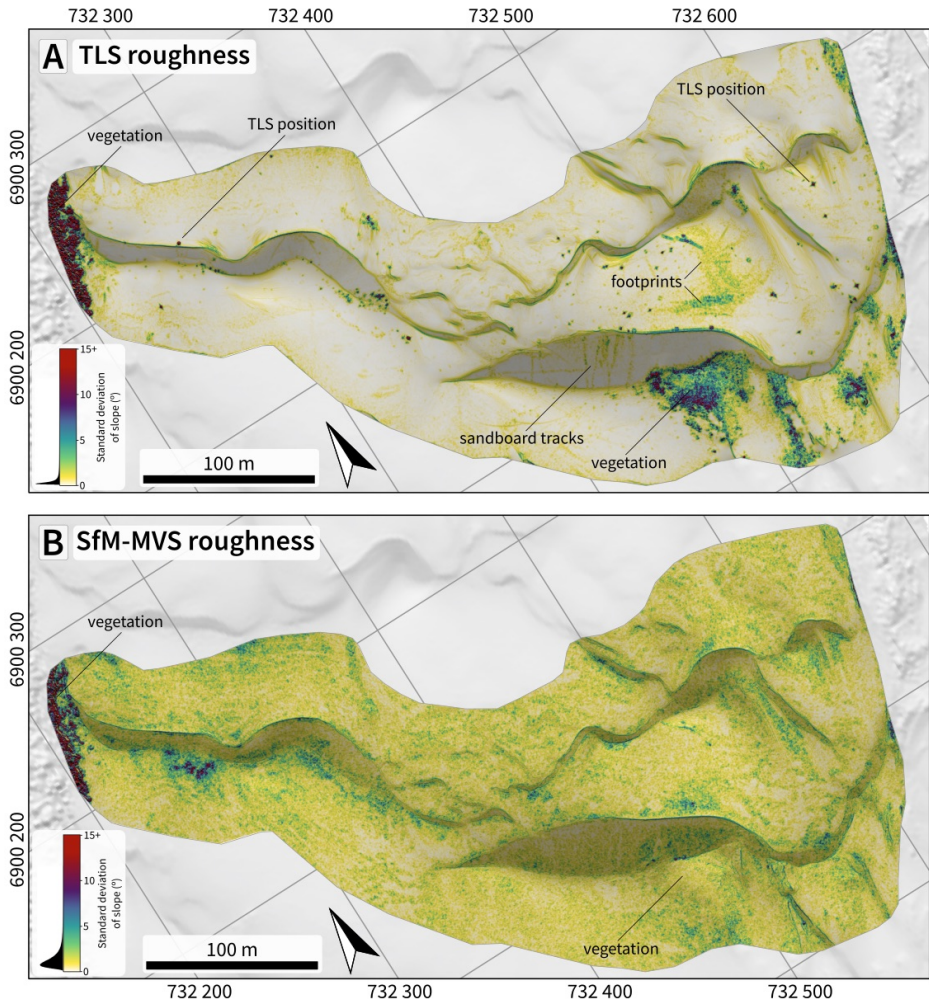


Figure 5: Surface roughness maps, calculated as the standard deviation of slope in a 5x5 window: A) TLS; B) SfM-MVS. Roughness colour scale is the same for A and B.

These results confirm the accuracy of the SfM-MVS reconstruction and validate its use for the dune migration and volume change analysis.

### 3.2. ALS and SfM-MVS

Besides a good correlation to the TLS DEM, the full SfM-MVS DEM (Fig. 7B) shows a good fit with elements of the landscape that didn't experienced significant change between the surveys, such as the road bordering the dune field to west and southwest (in grey in Fig. 7C, indicating no elevation difference).

Comparison of the 2010 ALS and 2019 SfM-MVS DEMs was carried out based on: 1)

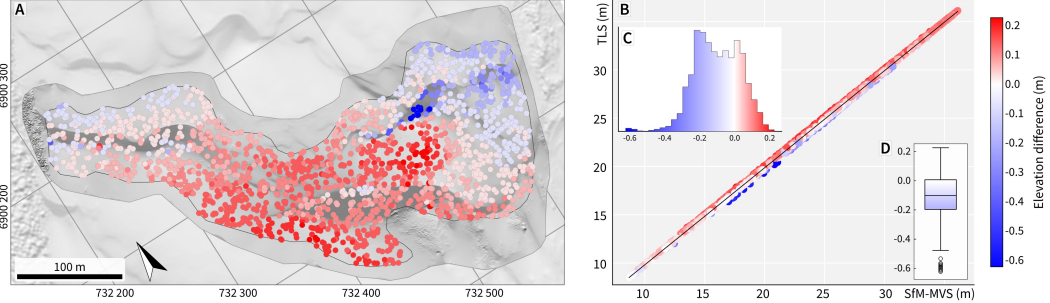


Figure 6: Differences between TLS and SfM-MVS: A) Map of difference values (2 000 random points); B) Scatterplot; C) Histogram (bins=26); D) Boxplot.

212 descriptive statistics of the DEMs; 2) differences between the DEMs; 3) sand volume within  
213 an area and 4) displacement of dune crests.

214 Differences between the DEMs were calculated by subtracting the elevations of the SfM-  
215 MVS DEM from the ALS DEM. Positive values represent areas where the SfM surface has  
216 higher elevations than the ALS one, and vice-versa.

217 The ALS and SfM-MVS DEMs (0.5 m resolution) and the differences between the two  
218 surfaces, are presented in Fig. 7. In the studied area, dunes are mainly barchanoids with  
219 lee side towards south west. Elevation reaches its highest ( $\approx 58$  m) in the southern portion,  
220 likely due the influence of an underlying palaeotopography (Giannini et al., 2007).

221 Descriptive statistics are presented in Table 3 and histograms of elevation values in Fig. 8.  
222 The DEM of differences between 2019 and 2010 DEMs is in Fig. 7C; positive values are in  
223 red and negative values in blue. Topographic profiles (location in Fig. 7B) are in Fig. 9.

224 The DEMs have similar values of maximum, standard deviation, skewness, kurtosis and  
225 quantiles. The SfM-MVS DEM shows slightly higher mean and minimum values; this can  
226 indicate an increase in sand volume over the north portion of the analysed area (marked #1  
227 in Fig. 7C), or local distortion of the modelled surface due a lack of GCPs on that region.

228 Elevation differences between the DEMs range from -16.80 m to +18.40 m, with mean  
229 and median above 0.0 m, a consequence of the higher minimum elevations of the SfM-MVS  
230 DEM. Some notable differences are indicated as #2,#3 and #4 in Fig. 7C: #2 marks the  
231 highest positive difference (where the SfM-MVS surface is above the ALS), related to the

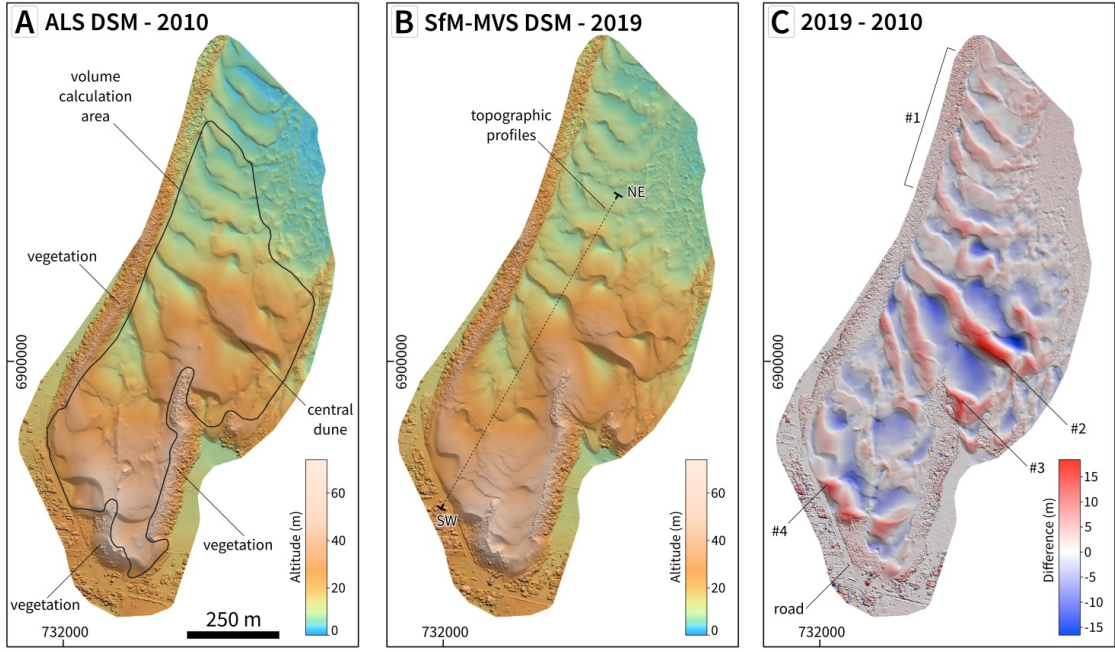


Figure 7: A) ALS DEM (2010), with volume calculation area polygon; B) SfM-MVS DEM (2019), with topographic profiles location; C) DEM of differences (2019-2010). Numbers in C are discussed in the text.

232 migration of a large ‘central dune’ with accumulation of sand towards a vegetated ridge in  
 233 #3; #4 shows the migration of the dune field over the road. In this place, the town hall  
 234 needs to remove the sand periodically to keep the road open.

Table 3: Descriptive statistics of the ALS, SfM-MVS DEMs and of differences between the two surfaces.

	min	max	mean	median	std.dev.	skewness	kurtosis	25%quant.	75%quant.
ALS	2.69	58.88	21.34	20.65	11.59	0.51	-0.41	11.64	28.77
SfM-MVS	4.70	58.55	22.06	20.95	11.21	0.51	-0.51	12.34	29.43
Diff.	-16.80	18.40	0.72	0.93	3.51	-0.08	2.45	-0.83	2.37

235 The polygon for volume calculation encloses only unvegetated areas in both surveys (see  
 236 Fig. 7A). Using the ALS and SfM DEMs with 0.5 m resolution, the calculated sand volumes  
 237 were 9 035 115.45 m<sup>3</sup> for 2010 and 9 081 185.49 m<sup>3</sup> for 2019 (an increase of 46 070.04 m<sup>3</sup> or  
 238 0.5%).

239 Dune crest displacement lines drawn over the DEMs (see Fig. 3) yielded a mean azimuth

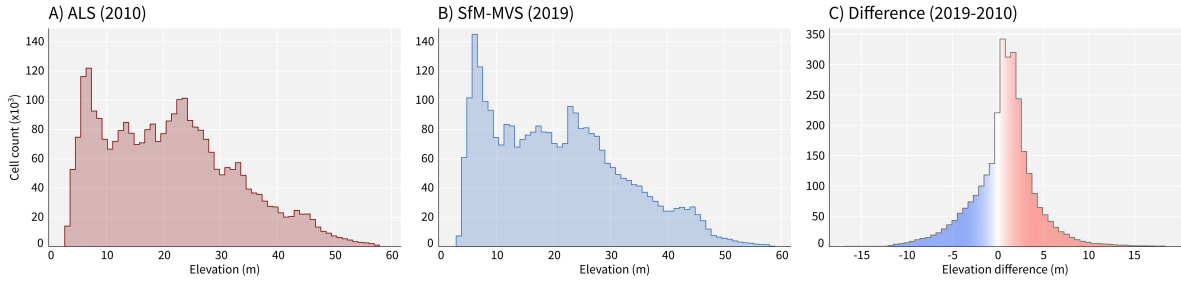


Figure 8: Histograms: A) ALS DEM (bins=60); SfM-MVS DEM (bins=60); C) DEM of differences (bins=40).

of  $215.5^\circ$  and mean length of  $\approx 44.5$  m (mean: 44.3 m, median: 44.7 m, see Supplemental Material for statistical analysis of azimuth and length).

A mean length of 44.5 m in 9 years corresponds to a dune migration rate of  $\approx 5$  m/year. We consider these rates to be in agreement with rates of 6-7 m/year from Mendes and Giannini (2015) and Mendes et al. (2015), which were derived from interpretation of historical aerial photographs and satellite images with coarser spatial resolution.

Topographic profiles (Fig. 9) illustrate dune movement from 2010 to 2019, with migration of the lee side and relatively less change over the stoss side of large compound dunes.

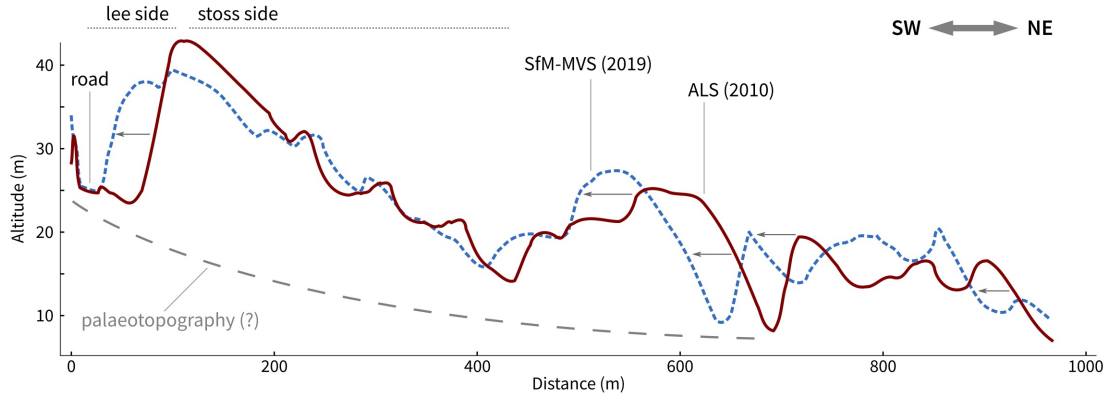


Figure 9: Topographic profiles across the dune field (location in Fig. 7B.)

248 **4. Discussions and Conclusions**

249 In this work, we presented a multi-source DEM analysis of dune migration and volume  
250 change. Data derived from an ALS DEM were compared to data from an SfM-MVS DEM  
251 and resulted in dune migration rate of  $\approx 5$  m/year and an increase of only 0.5% in sand  
252 volume between 2010 and 2019.

253 This migration rate is in good agreement with rates derived from satellite images and  
254 historical aerial photographs of the same area ([Mendes and Giannini, 2015](#); [Mendes et al.,  
255 2015](#)). The small positive change in volume can be related to the installation of sand fences  
256 to promote dune stabilization and decrease the need of sand removal from the front of the  
257 dune field (Fig. 10).

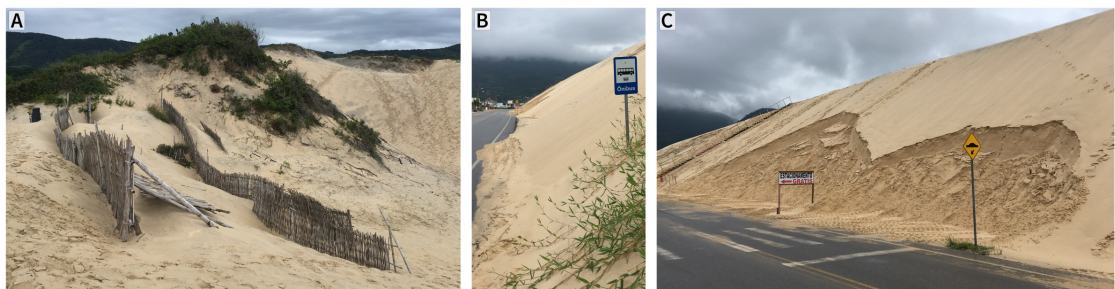


Figure 10: A) Sand fences installed to promote dune stabilization; B, C) Front of the dune field showing migration over road and signs. Location of photos on Fig. 2B.

258 To validate the use of an SfM-MVS DEM, a TLS DEM was used as reference for altimetric  
259 accuracy. The comparison was based on 2 000 random points and resulted in RMSE of  
260 0.16 m and MAE of 0.13 m, with SfM-MVS elevations slightly higher than the TLS ones.  
261 The TLS DEM has a smooth appearance, with well-marked dune crests and vegetated areas,  
262 while the SfM-MVS DEM shows a small-scale roughness that hinders visual identification of  
263 small features such as footprints. Although it does not influence the comparison with ALS  
264 data, this roughness can be an issue if the objective of the research is the classification of  
265 landforms based on geomorphometric parameters, such as the identification of dune crests  
266 based on surface curvature ([Mitasova et al., 2005b](#); [Hardin et al., 2014](#)).

267 Although sand dunes are commonly regarded as a challenge to traditional photogram-

268 metry due their homogeneous texture and spectral response, yielding poor results in image  
269 matching ([Baltsavias, 1999](#)), recent literature on close-range photogrammetry/SfM-MVS of  
270 coastal areas report good results in surface reconstruction ([Gonçalves and Henriques, 2015](#);  
271 [Gonçalves et al., 2018](#); [Duffy et al., 2018](#); [Laporte-Fauret et al., 2019](#); [van Puijenbroek et al.,  
272 2017](#); [Guisado-Pintado et al., 2019](#); [Pitman et al., 2019](#)).

273 In this research, image matching was successful in all areas of the survey due the presence  
274 of superficial features (footprints and sandboard tracks) and visibility of the sedimentary  
275 stratification, highlighted by heavy minerals (Fig. 2C).

276 One factor that positively influenced the UAV survey was the weather. A cloudy sky  
277 provided a diffuse illumination, without ‘hard’ shadows, and the scattered light rain ensured  
278 that the sand was humid, without the presence of a layer of loose sand over the dunes,  
279 which would mask the stratifications and other features in the photos ([Guisado-Pintado  
280 et al., 2019](#)).

281 We believe that the lack of texture in aerial photographs and satellite images is more  
282 related to ground resolution (i.e., pixel size) than the spectral or morphological character-  
283 istics of aeolian dunes, as a pixel area of one square metre can be enough to ‘average-out’  
284 small textural features and prevent good image matching. This is an issue to be seen in  
285 the context of the everlasting matter of scale in remote sensing and geomorphometry: pixel  
286 size *vs.* spatial structure (size) of landforms (e.g., [Woodcock and Strahler, 1987](#); [Wood,  
287 1996](#); [Gallant and Hutchinson, 1997](#); [Goodchild and Quattrochi, 1997](#); [Marceau and Hay,  
288 1999](#); [Hengl, 2006](#); [Kamal et al., 2014](#)). Large continental dunes, for instance, have been  
289 successfully modelled with 30 m-resolution images from Landsat and ASTER ([Levin et al.,  
290 2004](#); [Bullard et al., 2011](#)).

291 When comparing these different approaches to aeolian dune surface modelling (ALS,  
292 TLS and SfM-MVS) we must consider not only the accuracy of final products (DEMs), but  
293 also the time required to acquire the data and process it to a GIS-ready format.

294 ALS might be acquired in little time, but it is by far the most expensive, imposing a  
295 serious constrain on repeated surveys, especially for researchers in developing countries or  
296 without access to state-funded coastal monitoring programs.

297 TLS has an intermediate cost of acquisition (since the equipment can be rented and  
298 operated by the research team) but it demands more fieldwork and more processing time.  
299 In our case we needed three days for the TLS survey and around three weeks of full-time  
300 work to produce a DEM of  $\approx$ 80 400m<sup>2</sup>.

301 SfM-MVS has gained attention recently for being a low-cost solution with fast and reliable  
302 results (James et al., 2019). We were able to cover  $\approx$ 740 900m<sup>2</sup> with six UAV missions  
303 in under three hours. Processing time in a medium-range workstation (i.e., i7 processor,  
304 dedicated GPU) was  $\approx$ 13 hours. This makes it an excellent method for 3D modelling and  
305 continuous monitoring of coastal dunes.

306 One strength of the ALS over TLS and SfM-MVS is the possibility of removing the  
307 vegetation based on the laser returns or waveform (Evans and Hudak, 2007), although new  
308 methods are being developed for single-return point clouds (Guarnieri et al., 2009; Coveney  
309 et al., 2010; Coveney and Stewart Fotheringham, 2011; Montreuil et al., 2013; Pijl et al.,  
310 2020) that have been used in coastal environments with good results (Guisado-Pintado et al.,  
311 2019).

312 Another aspect to be considered is the weather. Dry and hot conditions will favour the  
313 presence of white sand patches, which can affect image matching and the 3D reconstruction.  
314 While clear sunny days might be seen by many as ideal conditions for fieldwork, flying the  
315 UAV with cloudy skies and after a light rain can be worthwhile due the scattered light and  
316 visibility of the dune's superficial features.

### 317 Acknowledgements

318 This study was supported by the Sao Paulo Research Foundation (FAPESP) grants  
319 #2009/17675-5 and #2016/06628-0 and by Brazil's National Council of Scientific and Tech-  
320 nological Development, CNPq grants #423481/2018-5 and #304413/2018-6 to C.H.G. This  
321 study was financed in part by CAPES Brasil - Finance Code 001 through PhD scholar-  
322 ships to G.P.B.G, A.A.A. and R.W.A. This work acknowledges the services provided by the  
323 OpenTopography Facility with support from the National Science Foundation under NSF

324 Award Numbers 1557484, 1557319, and 1557330. The authors are grateful to Clauson Lac-  
325 erda and Rodrigo Correa (FARO Technologies Brasil), for their continuous support with  
326 terrestrial LiDAR data processing. Acknowledgements are extended to the Editor-in-Chief  
327 and the anonymous reviewers for their criticism and suggestions, which helped to improve  
328 this paper.

329 **5. Supplementary material**

330       Supplementary data associated with this article can be found online at  
331       <http://dx.doi.org/10.0000/XXXXXX>.

332 **References**

- 333 Angulo, R., Lessa, G., Souza, M., 2006. A critical review of mid-to late-Holocene sea-level fluctuations on  
334 the eastern Brazilian coastline. Quaternary Science Reviews 25 (5-6), 486–506.
- 335 Baade, J., Schmullius, C., 2016. TanDEM-X IDEM precision and accuracy assessment based on a large  
336 assembly of differential GNSS measurements in Kruger National Park, South Africa. ISPRS Journal of  
337 Photogrammetry and Remote Sensing 119, 496 – 508.
- 338 Baltsavias, E. P., 1999. A comparison between photogrammetry and laser scanning. ISPRS Journal of  
339 Photogrammetry and Remote Sensing 54 (2-3), 83–94.
- 340 Bañón, L., Pagán, J. I., López, I., Banon, C., Aragonés, L., 2019. Validating UAS-Based Photogrammetry  
341 with Traditional Topographic Methods for Surveying Dune Ecosystems in the Spanish Mediterranean  
342 Coast. Journal of Marine Science and Engineering 7 (9).
- 343 Barnes, N., 2010. Publish your computer code: it is good enough. Nature 467 (7317), 753.
- 344 Baughman, C. A., Jones, B. M., Bodony, K. L., Mann, D. H., Larsen, C. F., Himelstoss, E., Smith, J., 2018.  
345 Remotely Sensing the Morphometrics and Dynamics of a Cold Region Dune Field Using Historical Aerial  
346 Photography and Airborne LiDAR Data. Remote Sensing 10 (5).
- 347 Bhadra, B. K., Rehpade, S. B., Meena, H., Srinivasa Rao, S., Sep 2019. Analysis of Parabolic Dune Morphom-  
348 etry and Its Migration in Thar Desert Area, India, using High-Resolution Satellite Data and Temporal  
349 DEM. Journal of the Indian Society of Remote Sensing.
- 350 URL <https://doi.org/10.1007/s12524-019-01050->
- 351 Bourke, M. C., Lancaster, N., Fenton, L. K., Parteli, E. J., Zimbelman, J. R., Radebaugh, J., 2010. Ex-  
352 traterrestrial dunes: An introduction to the special issue on planetary dune systems. Geomorphology

- 353 121 (1–2), 1 – 14.
- 354 URL <http://www.sciencedirect.com/science/article/pii/S0169555X10001868>
- 355 Brovelli, M. A., Cannata, M., 2004. Digital terrain model reconstruction in urban areas from airborne laser  
356 scanning data: the method and an example for Pavia (northern Italy). Computers & Geosciences 30,  
357 325–331.
- 358 Brovelli, M. A., Cannata, M., Longoni, U. M., 2004. LIDAR Data Filtering and DTM Interpolation Within  
359 GRASS. Transactions in GIS 8, 155–174.
- 360 Bullard, J. E., White, K., Livingstone, I., 2011. Morphometric analysis of aeolian bedforms in the Namib  
361 Sand Sea using ASTER data. Earth Surface Processes and Landforms 36 (11), 1534–1549.
- 362 Clemmensen, L. B., Bjørnsen, M., Murray, A., Pedersen, K., 2007. Formation of aeolian dunes on An-  
363 holt, Denmark since AD 1560: A record of deforestation and increased storminess. Sedimentary Geology  
364 199 (3–4), 171 – 187.
- 365 URL <http://www.sciencedirect.com/science/article/pii/S0037073807000486>
- 366 Conlin, M., Cohn, N., Ruggiero, P., 2018. A Quantitative Comparison of Low-Cost Structure from Motion  
367 (SfM) Data Collection Platforms on Beaches and Dunes. Journal of Coastal Research 34 (6), 1341–1357.
- 368 Coveney, S., Fotheringham, A. S., Charlton, M., McCarthy, T., 2010. Dual-scale validation of a medium-  
369 resolution coastal DEM with terrestrial LiDAR DSM and GPS. Computers & Geosciences 36 (4), 489 –  
370 499.
- 371 Coveney, S., Stewart Fotheringham, A., 2011. Terrestrial laser scan error in the presence of dense ground  
372 vegetation. The Photogrammetric Record 26 (135), 307–324.
- 373 Crosby, C. J., Arrowsmith, R. J., Nandigam, V., Baru, C., 2011. Geoinformatics. Cambridge University  
374 Press, Ch. Online access and processing of LiDAR topography data, p. 251–265.
- 375 Dong, P., 2015. Automated measurement of sand dune migration using multi-temporal lidar data and GIS.  
376 International Journal of Remote Sensing 36 (21), 5426–5447.
- 377 URL <https://doi.org/10.1080/01431161.2015.1093192>
- 378 Duffy, J. P., Shutler, J. D., Witt, M. J., DeBell, L., Anderson, K., 2018. Tracking Fine-Scale Struc-  
379 tural Changes in Coastal Dune Morphology Using Kite Aerial Photography and Uncertainty-Assessed  
380 Structure-from-Motion Photogrammetry. Remote Sensing 10 (9).
- 381 URL <https://www.mdpi.com/2072-4292/10/9/1494>
- 382 Evans, J. S., Hudak, A. T., 2007. A Multiscale Curvature Algorithm for Classifying Discrete Return LiDAR  
383 in Forested Environments. Geoscience and Remote Sensing, IEEE Transactions in 45, 1029–1038.
- 384 Fabbri, S., Giambastiani, B. M., Sistilli, F., Scarelli, F., Gabbianelli, G., 2017. Geomorphological analysis and  
385 classification of foredune ridges based on Terrestrial Laser Scanning (TLS) technology. Geomorphology  
386 295, 436 – 451.

- 387 FARO Technologies Inc., 2013. User Manual for the Focus3D 20/120 and S 20/120. Last access: 01/Jul/2019.
- 388 URL [https://knowledge.faro.com/Hardware/3D\\_Scanners/Focus/User\\_Manual\\_for\\_the\\_Focus3D\\_20-120\\_and\\_S\\_20-120?mt-learningpath=focus3d\\_20-120\\_downloads](https://knowledge.faro.com/Hardware/3D_Scanners/Focus/User_Manual_for_the_Focus3D_20-120_and_S_20-120?mt-learningpath=focus3d_20-120_downloads)
- 389
- 390 Feagin, R. A., Williams, A. M., Popescu, S., Stukey, J., Washington-Allen, R. A., 2014. The Use of Terrestrial
- 391 Laser Scanning (TLS) in Dune Ecosystems: The Lessons Learned. *Journal of Coastal Research*, 111–119.
- 392 URL <https://doi.org/10.2112/JCOASTRES-D-11-00223.1>
- 393 Finkel, H. J., 1961. The movement of barchan dunes measured by aerial photogrammetry. *Photogram Eng*
- 394 27, 439–444.
- 395 Fisher, N. I., 1993. Statistical Analysis of Circular Data. Cambridge Univ. Press, Cambridge.
- 396 Fryberger, S. G., Dean, G., 1979. A Study of Global Sand Seas. Vol. Prof. Paper 1052. U.S. Geological
- 397 Survey, Ch. Dune forms and wind regime, pp. 137–169.
- 398 Gallant, J., Hutchinson, M., 1997. Scale dependence in terrain analysis. *Mathematics and Computers in*
- 399 *Simulation* 43 (3), 313–322.
- 400 Gaylord, D. R., Foit, F. F., Schatz, J. K., Coleman, A. J., 2001. Smith Canyon dune field, Washington,
- 401 U.S.A: relation to glacial outburst floods, the Mazama eruption, and Holocene paleoclimate. *Journal of*
- 402 *Arid Environments* 47 (4), 403 – 424.
- 403 GDAL Development Team, 2019. GDAL - Geospatial Data Abstraction Library, Version 2.4.1. Open Source
- 404 Geospatial Foundation, Available at <http://gdal.osgeo.org>, last access 20-July-2019.,
- 405 Gesch, D. B., Oimoen, M. J., Danielson, J. J., Meyer, D., 2016. Validation of the ASTER Global Digital
- 406 Elevation Model version 3 over the conterminous United States. *International Archives of the Photogram-*
- 407 *metry, Remote Sensing and Spatial Information Sciences* XLI-B4, 143–148.
- 408 URL <http://pubs.er.usgs.gov/publication/70175051>
- 409 Giannini, P. C. F., Sawakuchi, A. O., Martinho, C. T., Tatumi, S. H., 2007. Eolian depositional episodes
- 410 controlled by Late Quaternary relative sea level changes on the Imbituba-Laguna coast (southern Brazil).
- 411 *Marine Geology* 237, 143–168.
- 412 Gonçalves, G. R., Pérez, J. A., Duarte, J., 2018. Accuracy and effectiveness of low cost UASs and open source
- 413 photogrammetric software for foredunes mapping. *International Journal of Remote Sensing* 39 (15-16),
- 414 5059–5077.
- 415 Gonçalves, J., Henriques, R., 2015. UAV photogrammetry for topographic monitoring of coastal areas.
- 416 *ISPRS Journal of Photogrammetry and Remote Sensing* 104, 101 – 111.
- 417 Goodchild, M., Quattrochi, D., 1997. Scale in Remote Sensing and GIS. CRC Press, Ch. Introduction: scale,
- 418 multiscaling, remote sensing and GIS, pp. 1–12.
- 419 GRASS Development Team, 2019. Geographic Resources Analysis Support System (GRASS GIS) Software,
- 420 Version 7.6. Open Source Geospatial Foundation.

- 421 URL <http://grass.osgeo.org>
- 422 Grohmann, C. H., 2004. Morphometric analysis in Geographic Information Systems: applications of free  
423 software GRASS and R. Computers & Geosciences 30, 1055–1067.
- 424 Grohmann, C. H., 2010. Coastal Dune Fields of Garopaba and Vila Nova, Santa Catarina State, Brazil.  
425 Airborne LiDAR. Data provided by FAPESP grant #2009/17675-5, distributed by OpenTopography, oT  
426 Collection ID: OT.032013.32722.1.
- 427 Grohmann, C. H., 2018. Evaluation of TanDEM-X DEMs on selected Brazilian sites: Comparison with  
428 SRTM, ASTER GDEM and ALOS AW3D30. Remote Sensing of Environment 212, 121 – 133.
- 429 Grohmann, C. H., 2019. Garopaba Dune Field, Santa Catarina State, Brazil. SfM-MVS point cloud.  
430 Data provided by FAPESP grant #2016/06628-0, distributed by OpenTopography, opentopoID:  
431 OTDS.072019.32722.1.
- 432 Grohmann, C. H., Garcia, G. P. B., Affonso, A. A., Albuquerque, R. W., 2019. Garopaba Dune Field, Santa  
433 Catarina State, Brazil. TLS point cloud. Data provided by FAPESP grant #2016/06628-0, distributed  
434 by OpenTopography, opentopoID: OTDS.102019.32722.1.
- 435 Grohmann, C. H., Riccomini, C., 2009. Comparison of roving-window and search-window techniques for  
436 characterising landscape morphometry. Computers & Geosciences 35, 2164–2169.
- 437 Grohmann, C. H., Sawakuchi, A. O., 2013. Influence of cell size on volume calculation using digital terrain  
438 models: A case of coastal dune fields. Geomorphology 180-181 (1), 130–136.
- 439 Grohmann, C. H., Smith, M. J., Riccomini, C., 2010. Multiscale Analysis of Topographic Surface Roughness  
440 in the Midland Valley, Scotland. Geoscience and Remote Sensing, IEEE Transactions on 49 (4), 1200–  
441 1213.
- 442 Guarnieri, A., Vettore, A., Pirotti, F., Menenti, M., Marani, M., 2009. Retrieval of small-relief marsh  
443 morphology from Terrestrial Laser Scanner, optimal spatial filtering, and laser return intensity. Geomor-  
444 phology 113 (1), 12 – 20, understanding earth surface processes from remotely sensed digital terrain  
445 models.
- 446 Guisado-Pintado, E., Jackson, D., Rogers, D., 2019. 3D mapping efficacy of a drone and terrestrial laser  
447 scanner over a temperate beach-dune zone. Geomorphology 328, 157–172.
- 448 Hardin, E., Mitasova, H., Tateosian, L., Overton, M., 2014. GIS-based Analysis of Coastal Lidar Time-Series.  
449 Springer New York.
- 450 Hayes, A., 2018. Dunes across the solar system. Science 360 (6392), 960–961, cited By 1.
- 451 Hayward, R., Mullins, K., Fenton, L., Hare, T., Titus, T., Bourke, M., Colaprete, A., Christensen, P.,  
452 2007. Mars global digital dune database and initial science results. Journal of Geophysical Research 112,  
453 E11007.
- 454 Hebeler, F., Purves, R. S., 2009. The influence of elevation uncertainty on derivation of topographic indices.

- 455 Geomorphology 111, 4–16.
- 456 Hengl, T., 2006. Finding the right pixel size. Computers and Geosciences 32 (9), 1283–1298.
- 457 Hengl, T., Reuter, H. I., 2008. Geomorphometry: Concepts, Software, Applications. Vol. 33 of Developments  
458 in Soil Science. Elsevier, Amsterdam.
- 459 Hesp, P., Abreu de Castilhos, J., Miot da Silva, G., Dillenburg, S., Martinho, C. T., Aguiar, D., Fornari,  
460 M., Fornari, M., Antunes, G., 2007. Regional wind fields and dunefield migration, southern Brazil. Earth  
461 Surface Processes and Landforms 32 (4), 561–573.
- 462 Hesp, P. A., Giannini, P. C. F., Martinho, C. T., Silva, G. M. D., Neto, N. E., 2009. The Holocene Barrier  
463 Systems of the Santa Catarina Coast, Southern Brazil. In: Dillenburg, S. R., Hesp, P. A. (Eds.), Geology  
464 and Geomorphology of Holocene Coastal Barriers of Brazil, Lecture Notes in Earth Sciences. Vol. 107.  
465 Springer Berlin / Heidelberg, pp. 93–133.
- 466 Hinckley, J., 1988. `r.volume` GRASS-GIS module. [accessed 05 December 2011].  
467 URL [http://grass.osgeo.org/grass64/manuals/html64\\_user/r.volume.html](http://grass.osgeo.org/grass64/manuals/html64_user/r.volume.html)
- 468 Hoover, R. H., Gaylord, D. R., Cooper, C. M., 2018. Dune mobility in the St. Anthony Dune Field, Idaho,  
469 USA: Effects of meteorological variables and lag time. Geomorphology 309, 29 – 37.
- 470 Hugenholtz, C. H., Barchyn, T. E., 2010. Spatial analysis of sand dunes with a new global topographic  
471 dataset: new approaches and opportunities. Earth Surface Processes and Landforms 35 (8), 986–992.  
472 URL <http://dx.doi.org/10.1002/esp.2013>
- 473 Hunter, J. D., May-Jun 2007. Matplotlib: A 2D graphics environment. Computing In Science & Engineering  
474 9 (3), 90–95.
- 475 Isenburg, M., 2019. LAStools - efficient LiDAR processing software (version 190623, unlicensed). Obtained  
476 from <http://rapidlasso.com/LAStools>.
- 477 James, M. R., Chandler, J. H., Eltner, A., Fraser, C., Miller, P. E., Mills, J. P., Noble, T., Robson, S., Lane,  
478 S. N., 2019. Guidelines on the use of structure-from-motion photogrammetry in geomorphic research.  
479 Earth Surface Processes and Landforms 44 (10), 2081–2084.
- 480 Judge, E. K., Courtney, M. G., Overton, M. F., 2000. Topographic analysis of dune volume and position,  
481 Jockey's Ridge State Park, North Carolina. Shore and Beach 68 (4), 19–24.
- 482 Kamal, M., Phinn, S., Johansen, K., 2014. Characterizing the Spatial Structure of Mangrove Features for  
483 Optimizing Image-Based Mangrove Mapping. Remote Sensing 6 (2), 984–1006.
- 484 Kluyver, T., Ragan-Kelley, B., Pérez, F., Granger, B., Bussonnier, M., Frederic, J., Kelley, K., Hamrick,  
485 J., Grout, J., Corlay, S., Ivanov, P., Avila, D., Abdalla, S., Willing, C., 2016. Positioning and Power in  
486 Academic Publishing: Players, Agents and Agendas. IOS Press, Ch. Jupyter Notebooks – a publishing  
487 format for reproducible computational workflows, pp. 87 – 90.
- 488 Kreslavsky, M. A., Bondarenko, N. V., 2017. Aeolian sand transport and aeolian deposits on Venus: A

- 489 review. Aeolian Research 26, 29–46, cited By 4.
- 490 Krishnan, S., Crosby, C., Nandigam, V., Phan, M., Cowart, C., Baru, C., Arrowsmith, R., 2011. OpenTo-  
491 pography: a services oriented architecture for community access to LIDAR topography. In: Proceedings  
492 of the 2nd International Conference on Computing for Geospatial Research & Applications. COM.Geo  
493 '11. ACM, New York, NY, USA, pp. 7:1–7:8.
- 494 Labuz, T. A., Apr 2016. A review of field methods to survey coastal dunes—experience based on research  
495 from South Baltic coast. Journal of Coastal Conservation 20 (2), 175–190.
- 496 Laporte-Fauret, Q., Marieu, V., Castelle, B., Michalet, R., Bujan, S., Rosebery, D., 2019. Low-Cost UAV  
497 for High-Resolution and Large-Scale Coastal Dune Change Monitoring Using Photogrammetry. Journal  
498 of Marine Science and Engineering 7 (3).
- 499 Lee, Y.-K., Eom, J., Do, J.-D., amd Joo-Hyung Ryu, B.-J. K., 2019. Shoreline Movement Monitoring and  
500 Geomorphologic Changes of Beaches Using Lidar and UAVs Images on the Coast of the East Sea, Korea.  
501 Journal of Coastal Research 90 (sp1), 409 – 414 – 6.
- 502 Levin, N., 2011. Climate-driven changes in tropical cyclone intensity shape dune activity on Earth's largest  
503 sand island. Geomorphology 125 (1), 239 – 252.
- 504 URL <http://www.sciencedirect.com/science/article/pii/S0169555X10004149>
- 505 Levin, N., Dor, B. E., Karnieli, A., 2004. Topographic information of sand dunes as extracted from shading  
506 effects using Landsat images. Remote Sensing of Environment 90 (2), 190–209.
- 507 Livingstone, I., Wiggs, G. F., Weaver, C. M., 2007. Geomorphology of desert sand dunes: A review of recent  
508 progress. Earth-Science Reviews 80 (3–4), 239 – 257.
- 509 URL <http://www.sciencedirect.com/science/article/pii/S0012825206001449>
- 510 Mancini, F., Dubbini, M., Gattelli, M., Stecchi, F., Fabbri, S., Gabbianelli, G., 2013. Using unmanned aerial  
511 vehicles (UAV) for high-resolution reconstruction of topography: The structure from motion approach on  
512 coastal environments. Remote Sensing 5 (12), 6880–6898.
- 513 Marceau, D. J., Hay, G. J., 1999. Remote sensing contributions to the scale issue. Canadian journal of  
514 remote sensing 25 (4), 357–366.
- 515 Martinho, C. T., Giannini, P. C. F., Sawakuchi, A. O., Hesp, P. A., 2006. Morphological and depositional  
516 facies of transgressive dunefields in the Imbituba-Jaguaruna region, Santa Catarina State. Journal of  
517 Coastal Research SI39, 143–168.
- 518 Martinho, C. T., Hesp, P. A., Dillenburg, S. R., 2010. Morphological and temporal variations of transgressive  
519 dunefields of the northern and mid-littoral Rio Grande do Sul coast, Southern Brazil. Geomorphology  
520 117 (1–2), 14 – 32.
- 521 URL <http://www.sciencedirect.com/science/article/pii/S0169555X0900467X>
- 522 McKinney, W., 2011. pandas: a Foundational Python Library for Data Analysis and Statistics. In: Python

- 523 for High Performance and Scientific Computing. pp. 1–9.
- 524 Mendes, V. R., Giannini, P. C. F., 2015. Coastal dunefields of south Brazil as a record of climatic changes  
525 in the South American Monsoon System. *Geomorphology* 246, 22 – 34.
- 526 Mendes, V. R., Giannini, P. C. F., Guedes, C. C. F., DeWitt, R., de Abreu Andrade, H. A., 08 2015. Central  
527 Santa Catarina coastal dunefields chronology and their relation to relative sea level and climatic changes.  
528 *Brazilian Journal of Geology* 45, 79 – 95.
- 529 Mitasova, H., Drake, T. G., Bernstein, D., Harmon, R. S., 2004. Quantifying Rapid Changes in Coastal  
530 Topography using Modern Mapping Techniques and Geographic Information System. *Environmental &*  
531 *Engineering Geoscience* 10, 1–11.
- 532 Mitasova, H., Mitas, L., Harmon, R. S., 2005a. Simultaneous spline approximation and topographic analysis  
533 for lidar elevation data in open source GIS. *IEEE Geoscience and Remote Sensing Letters* 2, 375–379.
- 534 Mitasova, H., Overton, M., Harman, R. S., 2005b. Geospatial analysis of a coastal sand dune field evolution:  
535 Jockey's Ridge, North Carolina. *Geomorphology* 72, 204–221.
- 536 Montreuil, A.-L., Bullard, J., Chandler, J., 2013. Detecting Seasonal Variations in Embryo Dune Morphology  
537 Using a Terrestrial Laser Scanner. *Journal of Coastal Research* 65 (SIv2), 1313–1318.
- 538 URL <https://doi.org/10.2112/SI65-222.1>
- 539 Neteler, M., Bowman, M. H., Landa, M., Metz, M., 2012. GRASS GIS: A multi-purpose open source GIS.  
540 *Environmental Modelling & Software* 31, 124–130.
- 541 Nikolakopoulos, K. G., Kamaratakis, E. K., Chrysoulakis, N., 2006. SRTM vs. ASTER elevation products.  
542 Comparison for two regions in Crete, Grece. *International Journal of Remote Sensing* 27, 4819–4838.
- 543 O'Dea, A., Brodie, K. L., Hartzell, P., 2019. Continuous Coastal Monitoring with an Automated Terrestrial  
544 Lidar Scanner. *Journal of Marine Science and Engineering* 7 (2).
- 545 Oliphant, T., 2006. Guide to NumPy. Trelgol Publishing.  
546 URL <http://www.tramy.us/>
- 547 Pagán, J., Bañón, L., López, I., Bañón, C., Aragonés, L., 2019. Monitoring the dune-beach system of  
548 Guardamar del Segura (Spain) using UAV, SfM and GIS techniques. *Science of the Total Environment*  
549 687, 1034–1045.
- 550 Pardo-Pascual, J., García-Asenjo, L., Palomar-Vázquez, J., Garrigues-Talens, P., 2005. New Methods and  
551 Tools to analyze beach-dune system evolution using a Real-Time Kinematic Global Positioning System  
552 and Geographic Information Systems. *Journal of Coastal Research*, 34–39.
- 553 URL <http://www.jstor.org/stable/25737401>
- 554 Pijl, A., Bailly, J.-S., Feurer, D., Maaoui, M. A. E., Boussema, M. R., Tarolli, P., 2020. TERRA: Terrain Ex-  
555 traction from elevation Rasters through Repetitive Anisotropic filtering. *International Journal of Applied*  
556 *Earth Observation and Geoinformation* 84, 101977.

- 557 Pike, R. J., 1995. Geomorphometry – progress, practice, and prospect. *Zeitschrift für Geomorphologie Suppl.*-  
 558 Bd. 101, 221–238.
- 559 Pike, R. J., Evans, I. S., Hengl, T., 2009. Chapter 1. Geomorphometry: a brief guide. In: Hengl, T., Reuter,  
 560 H. I. (Eds.), *Geomorphometry: Concepts, Software, Applications*. Vol. 33 of *Developments in Soil Science*.  
 561 Elsevier, Amsterdam, pp. 3–30.
- 562 Pitman, S. J., Hart, D. E., Katurji, M. H., 2019. Application of UAV techniques to expand beach research  
 563 possibilities: A case study of coarse clastic beach cusps. *Continental Shelf Research* 184, 44 – 53.
- 564 Potts, L. V., Akyilmaz, O., Braun, A., Shum, C. K., 2008. Multi-resolution dune morphology using Shuttle  
 565 Radar Topography Mission (SRTM) and dune mobility from fuzzy inference systems using SRTM and  
 566 altimetric data. *International Journal of Remote Sensing* 29 (10), 2879–2901.
- 567 URL <http://dx.doi.org/http://dx.doi.org/10.1080/01431160701408352>
- 568 Python Software Foundation, 2019. Python Programming Language, version 2.7.16. Available at  
 569 <http://www.python.org/>, last access 20-July-2019.
- 570 QGIS Development Team, 2019. QGIS Geographic Information System, Version 3.8. Open Source Geospatial  
 571 Foundation, Available at <http://qgis.org>, last access 20-July-2019.,
- 572 URL <http://qgis.org>
- 573 Radebaugh, J., Lorenz, R., Lunine, J., Wall, S., Boubin, G., Reffet, E., Kirk, R., Lopes, R., Stofan, E.,  
 574 Soderblom, L., Allison, M., Janssen, M., Paillou, P., Callahan, P., Spencer, C., the Cassini Radar Team,  
 575 2008. Dunes on Titan observed by Cassini Radar. *Icarus* 194 (2), 690 – 703.
- 576 URL <http://www.sciencedirect.com/science/article/pii/S001910350700512X>
- 577 Reuter, H. I., Hengl, T., Gessler, P., Soille, P., 2009. Chapter 4 Preparation of DEMs for Geomorphometric  
 578 Analysis. In: Hengl, T., Reuter, H. I. (Eds.), *Geomorphometry: Concepts, Software, Applications*. Vol. 33  
 579 of *Developments in Soil Science*. Elsevier, Amsterdam, pp. 87–120.
- 580 Rule, A., Tabard, A., Hollan, J. D., 2018. Exploration and Explanation in Computational Notebooks. In:  
 581 Proceedings of the 2018 CHI Conference on Human Factors in Computing Systems. CHI '18. ACM, New  
 582 York, NY, USA, pp. 32:1–32:12.
- 583 Satge, F., Denezine, M., Pillco, R., Timouk, F., Pinel, S., Molina, J., Garnier, J., Seyler, F., Bonnet, M.-  
 584 P., 2016. Absolute and relative height-pixel accuracy of SRTM-GL1 over the South American Andean  
 585 Plateau. *ISPRS Journal of Photogrammetry and Remote Sensing* 121, 157 – 166.
- 586 Sawakuchi, A. O., Kalchgruber, R., Giannini, P. C. F., Nascimento Jr, D. R., Guedes, C. C. F., Umisedo,  
 587 N. K., 2008. The development of blowouts and foredunes in the Ilha Comprida barrier (Southeastern  
 588 Brazil): the influence of Late Holocene climate changes on coastal sedimentation. *Quaternary Science  
 589 Reviews* 27, 2076 – 2090.
- 590 Seymour, A., Ridge, J., Rodriguez, A., Newton, E., Dale, J., Johnston, D., 2018. Deploying Fixed Wing

- 591 Unoccupied Aerial Systems (UAS) for Coastal Morphology Assessment and Management. *Journal of*  
592 *Coastal Research* 34 (3), 704 – 717.
- 593 Short, A. D., 1988. Holocene coastal dune formation in southern australia: A case study. *Sedimentary*  
594 *Geology* 55 (1–2), 121 – 142.
- 595 URL <http://www.sciencedirect.com/science/article/pii/0037073888900930>
- 596 Shrestha, R. L., Carter, W. E., Sartori, M., Luzum, B. J., Slatton, K. C., 2005. Airborne Laser Swath  
597 Mapping: Quantifying changes in sandy beaches over time scales of weeks to years. *ISPRS Journal of*  
598 *Photogrammetry and Remote Sensing* 59 (4), 222–232.
- 599 Singhvi, A., Williams, M., Rajaguru, S., Misra, V., Chawla, S., Stokes, S., Chauhan, N., Francis, T., Ganjoo,  
600 R., Humphreys, G., 2010. A ~200 ka record of climatic change and dune activity in the Thar Desert,  
601 India. *Quaternary Science Reviews* 29 (23–24), 3095 – 3105.
- 602 URL <http://www.sciencedirect.com/science/article/pii/S027737911000291X>
- 603 Smith, M. W., Vericat, D., 2015. From experimental plots to experimental landscapes: topography, ero-  
604 sion and deposition in sub-humid badlands from Structure-from-Motion photogrammetry. *Earth Surface*  
605 *Processes and Landforms* 40 (12), 1656–1671.
- 606 Solazzo, D., Sankey, J., Sankey, T., Munson, S., 2018. Mapping and measuring aeolian sand dunes with  
607 photogrammetry and LiDAR from unmanned aerial vehicles (UAV) and multispectral satellite imagery  
608 on the Paria Plateau, AZ, USA. *Geomorphology* 319, 174–185.
- 609 Stafford, D. B., Langfelder, J., 1971. Air photo survey of coastal erosion. *Photogrammetric engineering*  
610 37 (6), 565–575.
- 611 Stevenson, J. A., Sun, X., Mitchell, N. C., 2010. Despeckling SRTM and other topographic data with a  
612 denoising algorithm. *Geomorphology* 114 (3), 238–252.
- 613 URL <http://dx.doi.org/10.1016/j.geomorph.2009.07.006>
- 614 Sun, X., Rosin, P., Martin, R., Langbein, F., Sept 2007. Fast and Effective Feature-Preserving Mesh De-  
615 noising. *IEEE Transactions on Visualization and Computer Graphics* 13 (5), 925–938.
- 616 Taddia, Y., Corbau, C., Zambello, E., Pellegrinelli, A., 2019. UAVs for structure-from-motion coastal mon-  
617 itoring: A case study to assess the evolution of embryo dunes over a two-year time frame in the po river  
618 delta, Italy. *Sensors (Switzerland)* 19 (7).
- 619 Telfer, M. W., Parteli, E. J., Radebaugh, J., Beyer, R. A., Bertrand, T., Forget, F., Nimmo, F., Grundy,  
620 W. M., Moore, J. M., Stern, S. A., et al., 2018. Dunes on Pluto. *Science* 360 (6392), 992–997.
- 621 The SciPy community, October 2013. SciPy Reference Guide – Release 0.13.0.
- 622 URL <http://docs.scipy.org/doc/scipy/scipy-ref.pdf>
- 623 Tsoar, H., Levin, N., Porat, N., Maia, L. P., Herrmann, H. J., Tatumi, S. H., Claudino-Sales, V., 2009. The  
624 effect of climate change on the mobility and stability of coastal sand dunes in Ceará State (NE Brazil).

- 625 Quaternary Research 71 (2), 217 – 226.
- 626 URL <http://www.sciencedirect.com/science/article/pii/S0033589408001464>
- 627 van Puijenbroek, M. E. B., Nolet, C., de Groot, A. V., Suomalainen, J. M., Riksen, M. J. P. M., Berendse,  
628 F., Limpens, J., 2017. Exploring the contributions of vegetation and dune size to early dune development  
629 using unmanned aerial vehicle (UAV) imaging. Biogeosciences 14 (23), 5533–5549.
- 630 Viana, C. D., Grohmann, C. H., Busarello, M., Garcia, G. P. B., 12 2018. Structural analysis of clastic dikes  
631 using Structure from Motion - Multi-View Stereo: a case-study in the Paraná Basin, southeastern Brazil.  
632 Brazilian Journal of Geology 48, 839 – 852.
- 633 Wang, X., Dong, Z., Zhang, J., Chen, G., 2002. Geomorphology of sand dunes in the Northeast Taklimakan  
634 Desert. Geomorphology 42 (3–4), 183 – 195.
- 635 URL <http://www.sciencedirect.com/science/article/pii/S0169555X0100085X>
- 636 Waskom, M., Botvinnik, O., drewokane, Hobson, P., David, Halchenko, Y., Lukauskas, S., Cole, J. B.,  
637 Warmenhoven, J., de Ruiter, J., Hoyer, S., Vanderplas, J., Villalba, S., Kunter, G., Quintero, E., Martin,  
638 Miles, A., Meyer, K., Augspurger, T., Yarkoni, T., Bachant, P., Williams, M., Evans, C., Fitzgerald,  
639 C., Brian, Wehner, D., Hitz, G., Ziegler, E., Qalieh, A., Lee, A., Jun. 2016. seaborn: v0.7.1 (june 2016).
- 640 Wechsler, S. P., 2007. Uncertainties associated with digital elevation models for hydrologic applications: a  
641 review. Hydrology and Earth System Sciences 11 (4), 1481–1500.
- 642 Westoby, M. J., Brasington, J., Glasser, N. F., Hambrey, M. J., Reynolds, J. M., 2012. ‘Structure-from-  
643 Motion’ photogrammetry: A low-cost, effective tool for geoscience applications. Geomorphology 179,  
644 300–314.
- 645 Willmott, C. J., Matsuura, K., 2005. Advantages of the mean absolute error (MAE) over the root mean  
646 square error (RMSE) in assessing average model performance. Clim Res 30 (1), 79–82.
- 647 Willmott, C. J., Matsuura, K., 2006. On the use of dimensioned measures of error to evaluate the performance  
648 of spatial interpolators. International Journal of Geographical Information Science 20 (1), 89–102.
- 649 Wood, J., 1996. Scale-based characterization of Digital Elevation Models. In: Parker, D. (Ed.), Innovations  
650 in GIS 3. London: Taylor and Francis, Ch. 13.
- 651 Woodcock, C. E., Strahler, A. H., 1987. The factor of scale in remote sensing. Remote Sensing of Environment  
652 21 (3), 311 – 332.
- 653 Yang, J., Dong, Z., Liu, Z., Shi, W., Chen, G., Shao, T., Zeng, H., 2019. Migration of barchan dunes in the  
654 western Quruq Desert, northwestern China. Earth Surface Processes and Landforms 44 (10), 2016–2029.
- 655 Zambelli, P., Gebbert, S., Ciolli, M., 2013. Pygrass: An Object Oriented Python Application Programming  
656 Interface (API) for Geographic Resources Analysis Support System (GRASS) Geographic Information  
657 System (GIS). ISPRS International Journal of Geo-Information 2 (1), 201–219.

658    **Notes**

- 659    <sup>1</sup><https://spectrageospatial.com/survey-office>  
660    <sup>2</sup>[https://knowledge.faro.com/Software/FARO\\_SCENE/SCENE](https://knowledge.faro.com/Software/FARO_SCENE/SCENE)  
661    <sup>3</sup><https://support.dronesmadeeasy.com>  
662    <sup>4</sup><https://www.agisoft.com>  
663    <sup>5</sup>[https://github.com/CarlosGrohmann/scripts\\_papers/tree/master/garopaba\\_als\\_sfm\\_tls](https://github.com/CarlosGrohmann/scripts_papers/tree/master/garopaba_als_sfm_tls)  
664    <sup>6</sup><https://doi.org/10.5281/zenodo.3476779>  
665    <sup>7</sup><http://opentopo.sdsc.edu>